# Optoelectronics of Atomic Metal-Semiconductor Interfaces in Tin-Intercalated MoS<sub>2</sub>

Avraham Twitto, <sup>1,2,†</sup> Chen Stern, <sup>1,2,†</sup> Michal Poplinger, <sup>1,2</sup> Ilana Perelshtein, <sup>2</sup> Sabyasachi Saha, <sup>4,7</sup> Akash Jain, <sup>5</sup> Kristie J. Koski, <sup>3</sup> Francis Leonard Deepak, <sup>4</sup> Ashwin Ramasubramaniam, <sup>6</sup> and Doron Naveh <sup>1,2,\*</sup>

#### Abstract

Metal-semiconductor interfaces are ubiquitous in modern electronics. These quantum-confined interfaces allow for the formation of atomically-thin polarizable metals and feature rich optical and optoelectronic phenomena, including plasmon-induced hot-electron transfer from metal to semiconductors. Here, we report on the metal–semiconductor interface formed during the intercalation of zerovalent atomic layers of tin (Sn) between layers of  $MoS_2$ , a van der Waals layered material. We demonstrate that Sn interaction leads to the emergence of gap states within the  $MoS_2$  bandgap and new plasmonic features between 1-2 eV (0.6–1.2  $\mu$ m). The observed stimulation of the photoconductivity, as well as the extension of the spectral response from the visible regime towards the mid-infrared suggests that hot-carriers generation and internal photoemission take place.

*Keywords:* intercalation, plasmonic enhancement, photoconductive gain, light-matter interaction, internal photoemission, hot-carrier injection, metal–semiconductor interface

#### Introduction

Interfaces of metals and semiconductors have attracted great scientific interest since the beginning of the 20<sup>th</sup> century. These interfaces are ubiquitous in modern electronic devices and provide a technological motivation for studying the rich physics originating at the boundary of localized and delocalized electrons. The progress of nano-plasmonics over the last two decades and the emergence of nano-scaled metal-semiconductor interfaces (MSIs) has further provided

<sup>&</sup>lt;sup>1</sup> Faculty of Engineering, Bar-Ilan University, Ramat Gan, Israel

<sup>&</sup>lt;sup>2</sup> Institute for Nanotechnology and Advanced Materials, Bar-Ilan University, Ramat Gan, Israel

<sup>&</sup>lt;sup>3</sup> Department of Chemistry, University of California, Davis, USA

<sup>&</sup>lt;sup>4</sup> Nanostructured Materials Group, International Iberian Nanotechnology Laboratory, Braga, Portugal

<sup>&</sup>lt;sup>5</sup> Department of Chemical Engineering, University of Massachusetts, Amherst, MA 01003, USA

<sup>&</sup>lt;sup>6</sup> Department of Mechanical and Industrial Engineering, University of Massachusetts, Amherst, MA 01003, USA

<sup>&</sup>lt;sup>7</sup> CEMES-CNRS, 29 Rue Jeanne Marvig, 31055 Toulouse, France

<sup>\*</sup> Corresponding author: doron.naveh@biu.ac.il

<sup>&</sup>lt;sup>†</sup> The authors contributed equally to this paper

a wealth of outstanding physical and chemical observations. <sup>1-3</sup> In nano-scaled junctions, the near-field plasmonic enhancement of the electromagnetic wave – where the evanescent decay length is on the same scale of the MSI itself – enables the harvesting of hot electrons injected from the plasmonic metal to the conduction band of the semiconductor, leaving behind hot holes.<sup>4, 5</sup> This process requires that the thermal energy and momentum of the electrons are sufficient to cross the energy barrier of the MSI. In some cases, new plasmonic states that do not occur in either the metal or semiconductor alone can emerge at an MSI <sup>3, 6, 7</sup>. Transport of plasmonic hot carriers (HCs) at MSIs is considered to be a promising operating mechanism of future photovoltaic, photocatalysis and photodetection devices <sup>4-8</sup>. The efficiency of such devices depends on the efficiency of HC injection that is limited by the Schottky barrier height and by the mean free path (MFP) of the HCs <sup>2, 9</sup>.

In this paper, we present atomic-scale MSIs achieved by intercalation of Sn atoms into the van der Waals (vdW) gap of MoS<sub>2</sub>. We show that monolayer Sn, confined within the dielectric and chemical environment of the MoS<sub>2</sub> vdW gap, features an MSI-induced plasmonic signature. This is analogous to the cases of gallium and indium intercalated between graphene and SiC substrates <sup>10</sup>, wherein unexpected plasmonic behavior <sup>11</sup>, arising from quantum confinement and symmetry breaking along the out-of-plane direction <sup>12, 13</sup>, was reported. The intercalation of atomically-thin Sn layers results in the thinnest possible MSI. Enabled by the unique electronic structure of this MSI, we demonstrate photodetectors (photodiodes) with high responsivity that realize the predicted promise of such plasmonic MSIs over the past two decades <sup>14-17</sup>. Furthermore, the spectral response of the photodiodes is extended from the visible (MoS<sub>2</sub> only) towards the mid-infrared (Sn-intercalated MoS<sub>2</sub>), thereby confirming the mechanism of internal photoemission. Our results offer avenues for designing ultracompact, next-generation photodetectors and sensors based on intercalated van der Waals materials.

#### Results and Discussions

Atomic layers of Sn intercalated into CVD-grown vertical MoS<sub>2</sub> organize as islands on the scale of ~20 nm (Figure 1). Similar to the intercalation of Ga and In <sup>10, 11</sup>, the electronic structure of atomically-thin Sn clusters are subjected to strong localization due to quantum confinement. Figure 1a displays an HRTEM micrograph of MoS<sub>2</sub> after intercalation, showing the presence of Sn atoms arranged as atomically-thin layers between the MoS<sub>2</sub> planes. The intercalationinduced deformation within the crystalline structure of MoS<sub>2</sub> can be inferred from Figure S4b, which shows the distribution of the MoS<sub>2</sub> interplanar spacing, as well as from the line profile of Figure 1c that is associated with the yellow marked area in Figure 1b. The average interplanar spacing is found to increase after Sn intercalation from 0.631 nm to 0.639 nm – a total expansion of 1.3%. This expansion is also illustrated in the high-magnification micrograph in Figure 1a and Figure 1b that shows the presence of an additional plane of Sn atoms between two consecutive (0002) planes of MoS<sub>2</sub>. Figure 1c presents the line profile from the area enclosed by the yellow rectangle of Figure 1b, showing the average arrangement of Sn within MoS<sub>2</sub> layers. The Sn is found to be distributed throughout the host material and intercalated more or less evenly between layers. The presence of Sn in MoS<sub>2</sub> is further confirmed from the Sn peaks seen in the EDS spectra (Figure S2) acquired from the regions shown in Figure 1b. The Sn concentration is found to be 3.4 +/- 0.1 atomic percent, spatially arranged as clusters as can be inferred from Figure S1.

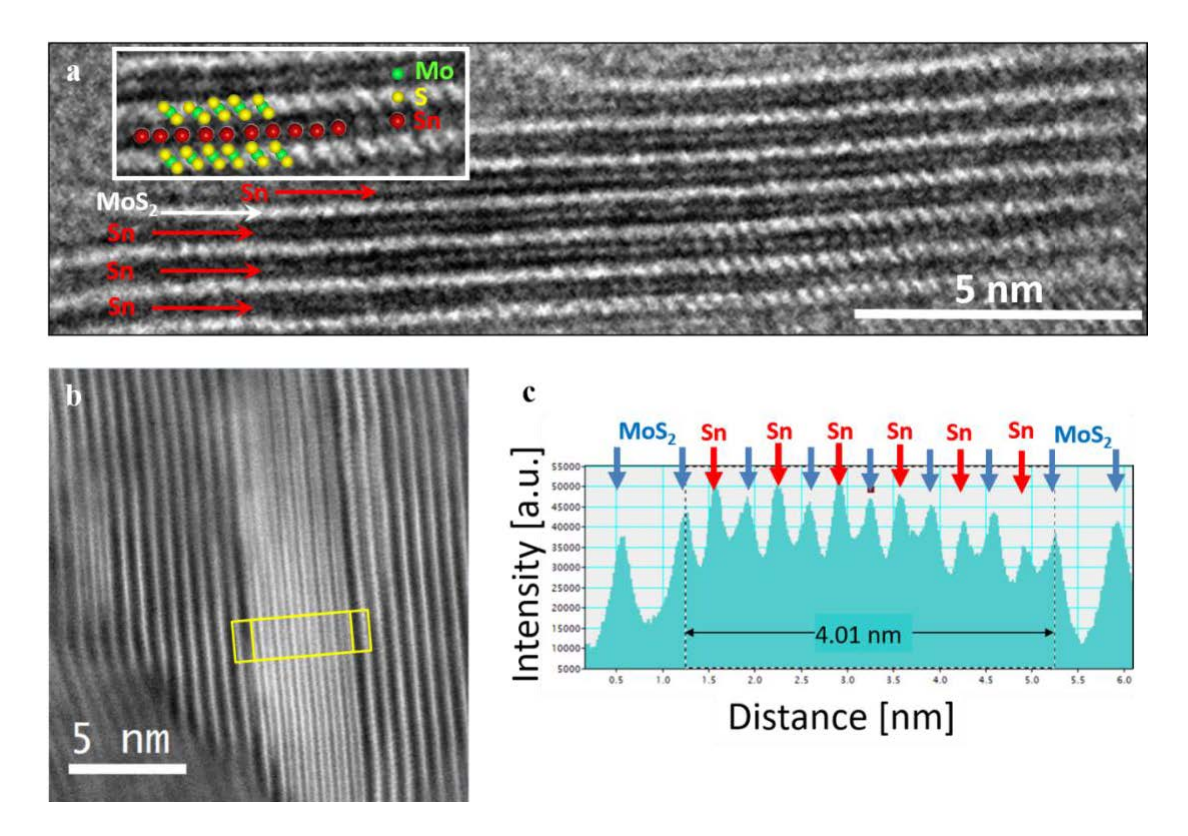


**Figure 1.** Structural characterization of MoS<sub>2</sub> intercalated with zerovalent Sn atoms: (a) HRTEM image with an inset displaying a single intercalated Sn layer within the van der Waals gap between two MoS<sub>2</sub> layers (Sn atoms are highlighted in red, while S and Mo are highlighted in yellow and green, respectively); (b) STEM-HAADF image showing the periodic intensity contrast with Mo or Sn appearing with bright contrast of parallel sets of planes; (c) the intensity profile across the marked rectangle in (b) with blue arrows indicating the Mo layer and red arrows indicating the intercalated Sn layer.

Raman spectra obtained with a 532 nm laser oriented parallel to the c-axis of the crystal display the expected modes of 2H-MoS<sub>2</sub>, with some stiffening of the A<sub>1g</sub> mode (Figure S3) that results from the intercalation of Sn. Raman modes can show complex softening or stiffening, depending upon the expansion or contraction of the host lattice as well as the electron donor/acceptor nature of the intercalant. A shift in the Raman mode with intercalation supports evidence of a change in the nature of the interlayer vdW gap as seen in Figure S4b and the calculations of Figure S4a. The increase in the Raman wave shift is consistent with optical phonon stiffening and has been observed in other intercalated systems <sup>19,18</sup>. Interestingly, the structure of Sn intercalation differs significantly from that of MoS<sub>2</sub> intercalated with copper <sup>3</sup> or lithium <sup>13, 20</sup>, as well as from that of In and Ga in graphene-SiC <sup>10, 21</sup>, as in all of these cases, the intercalant forms continuous layers, whereas Sn adopts a predominantly island-like structure. The structure inferred from HRTEM confirms the arrangement of Sn as single atom thick islands of 20-50 nm, consistent with the Rüdorff mechanism of intercalation <sup>22</sup>. The intercalation energy (Eq. S1) estimates the driving force for clustering of Sn atoms and is reflected by the trend displayed in Figure S4a. Initially, the relatively large diameter of Sn atoms requires overcoming a sizable thermodynamic barrier, calculated to be in the range of 3.5 eV/atom (see SI for details on DFT calculations), to intercalate within the vdW gap. From this point onwards, the "wedging" action of the initial intercalation event(s) allows for more facile intercalation of additional Sn atoms, resulting in a rapid decrease and eventual saturation of the thermodynamic barrier for continued Sn intercalation. Complementarily, most of the c-axis expansion that results from the intercalation process is affected by the initial intercalation event(s) and remains largely unaffected after the formation of small Sn clusters (Figure S4a).

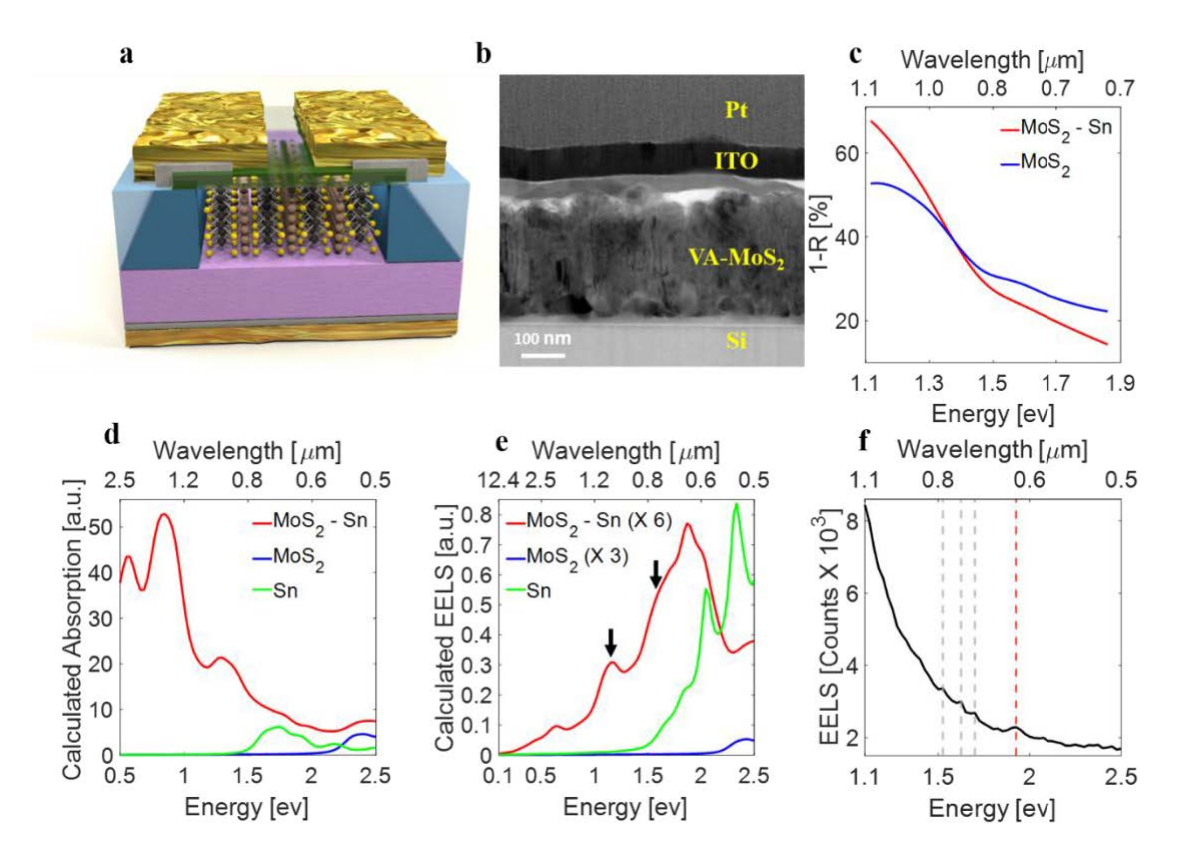


**Figure 2.** (a) Graphical illustration of the cross-section of a VA- MoS2 (yellow and black atoms), Si (light blue) heterostructure photodiode device intercalated by Sn (light brown atoms). (b) Bright Field Transmission electron microscope (TEM) micrograph of the Cross-section of the device structure. Comparison I-V of the two types of devices with and without Sn intercalation. (c) Measured absorption spectrum of a Sn-intercalated MoS<sub>2</sub> device (red line) and the pristine MoS<sub>2</sub> device (blue line). (d) Absorption spectra and (e) EELS spectra of MoS<sub>2</sub>+Sn<sub>ML</sub> (red line), bulk MoS<sub>2</sub> (blue line) and the isolated Sn monolayer (green line) calculated using the hybrid HSE functional (see Computational Methods in SI). Plasmonic features in the EELS spectrum of MoS<sub>2</sub>+Sn<sub>ML</sub> are highlighted with arrows. (f) Low-loss EELS spectrum obtained from the Sn-intercalated MoS<sub>2</sub> sample.

The impact of Sn intercalation on the optical properties of  $MoS_2$  is inferred from the measured and calculated optical absorption (**Figure 2c and 2d**). The measured absorption spectra of pristine and Sn-intercalated  $MoS_2$  (**Figure 2c**) cross at ~1.35 eV, which is close to the (indirect) bandgap of bulk  $MoS_2$ .<sup>23</sup> The Sn-intercalated  $MoS_2$  samples also display a sharp increase in absorption at lower energies, which is qualitatively consistent with the calculated absorption spectrum for bulk  $MoS_2$  with an intercalated Sn monolayer ( $MoS_2+Sn_{ML}$ ; **Figure 2d**). The electron energy loss (EELS) spectra (**Figure 2e** and **2f**) clearly show a primary peak at ~2.0 eV for the Sn-intercalated  $MoS_2$  samples: this peak is close in energy to the experimentally measured exciton of  $MoS_2$  and, moreover, is calculated to be close in energy to the single-particle excitation energies of both bulk  $MoS_2$  and the Sn monolayer (see **Figure S6**). In addition, several weak energy-loss features appear consistently in our measurements (grey dashed lines in **Figure 2f**) and DFT calculations (**Figure 2e**). In particular, the DFT calculations indicate that the shoulder in the EELS spectrum near 1.6 eV is plasmonic in nature, as is the peak near 1.1 eV (see **Figure S6**). These features are entirely absent—either as collective or

single-particle excitations—from the calculated EELS of bulk  $MoS_2$ , thus indicating that these plasmons are an emergent property of the hybrid material formed upon Sn intercalation in  $MoS_2$ . A more sophisticated analysis of single-particle versus collective excitations beyond the independent-particle picture  $^{25, 26}$  is beyond the scope of this work and will be pursued elsewhere.

In order to understand the optoelectronic properties of Sn-intercalated MoS<sub>2</sub>, we fabricated a diode on a p-Si substrate (see graphical illustration in Figure 2a and device cross-section in Figure 2b) with a top contact of semi-transparent ITO. The details of the fabrication can be found in the Methods section. The monochromatic (850 nm) photocurrent and responsivity (the ratio of photocurrent to illumination power) as a function of illumination power are compared systematically between the cases of pristine MoS<sub>2</sub> and Sn-intercalated MoS<sub>2</sub> in Figure 3a. The peculiar non-monotonic trend of the responsivity with respect to the power (Figure 3a) suggests the possibility of some thermal stimulation of the photoresponse. Complementing the latter observation of the responsivity, the photoconductive spectral response of the intercalated device (Figure 3b) shows an additional broad peak at ~1.3 μm followed by a broader signature that extends towards the mid infrared. This behavior aligns well with the calculated absorption and EELS spectra (Figure 2d, 2e). Initially, the pristine MoS<sub>2</sub> device already features a sizable photoconductive gain that is attributed to the orientation of the crystal<sup>27</sup> and with hot photocarriers generated at shallow defects of dislocations and grain boundaries. We attribute the enhanced photoconductive gain and infrared enhancement to the confined Sn-MoS<sub>2</sub> MSI. These hybrid MSI states extend from the band edges of pristine MoS<sub>2</sub>, enabling efficient ionization of carriers from metal-hybrid states into the conduction band upon optical excitation. Interestingly, we observe a non-monotonic relation of the responsivity with respect to the incident illumination power (Figure 3a), indicative of a gain mechanism involving thermal effects that is are line with the character of metallic Sn clusters.

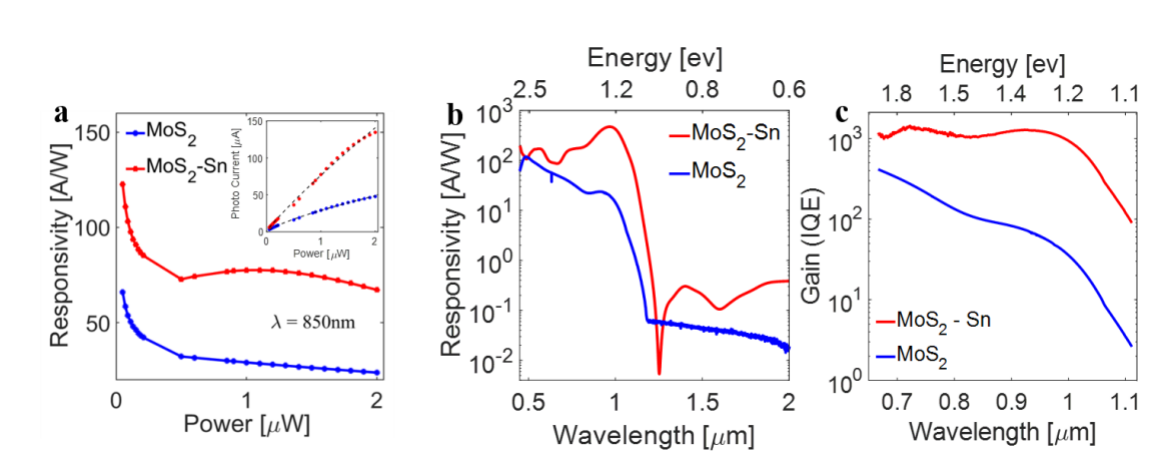


**Figure 3.** (a) Responsivity as a function of incident power of the Sn-intercalated MoS<sub>2</sub> device (red line) and the pristine MoS<sub>2</sub> device (blue line) under illumination of 850 nm at a reverse bias of -2V (Inset: Dependence of photocurrent on incident power at wavelength of 850 nm). (b) Responsivity vs. wavelength of the Sn-intercalated MoS<sub>2</sub> device (red line) and the pristine MoS<sub>2</sub> device (blue line). (c) Gain vs. wavelength of the Sn-intercalated MoS<sub>2</sub> device (red line) and the pristine MoS<sub>2</sub> device (blue line).

The internal quantum efficiency (IQE), i.e., the spectral photoconductive gain of the devices is displayed in **Figure 3c**. Since the upper bound of IQE is unity, we attribute the excess of

electrons collected per photon to a photoconductive gain. The photoconductive gain (**Figure 3c**) in the 0.7–1.1µm wavelength range attains peak values of ~400 and ~1400 for the pristine and Sn-intercalated MoS<sub>2</sub> devices, respectively. Considering the response time of the devices (~10 µs) and their IR-extended spectral response, we attribute the observed photoconductive gain to internal photoemission processes from the newly-formed Sn-MoS<sub>2</sub> MSIs. The magnitude of HC injection is proportional to their mean free path, scaling as  $\lambda_{el}(E) \propto \frac{1}{E^2}$ , where  $\lambda_{el}$  is the electron mean free path and E is the electron thermal energy, ranging from 0 to  $\hbar\omega$  (the exciting photon energy). <sup>15, 28, 29</sup> However, unlike the case of Schottky diodes, where a threshold energy exists for HC injection (the barrier height), <sup>30, 31</sup> here the MSI geometry is parallel to the applied electric field such that the HC can drift without having to overcome an energy barrier across the MSI. Furthermore, the interface length scale is orders of magnitude shorter than the mean free path of HCs, resulting in efficient collection of the photocurrent below the MoS<sub>2</sub> bandgap.

**Table 1.** Comparison of the characteristics of Si/MoS<sub>2</sub> photodetectors reported in this work and those in previous reports (VA – vertically-aligned).

Device	Responsivity	Wavelength	Response Time	Ref.
	(A/W)	(nm)	(rise/fall)	
Si/Sn-VA-	467-0.26	450-1600	13.4/12.1 μs	This work
$MoS_2$	max: 467	966		THIS WOLK
Si/VA-MoS2	117-0.07	450-1180	5.2/1.2 μs	This work
St/ VA-MOS2	max: 117	486		THIS WOLK
Si/ Cu- VA-	1301-46	485-1100	16.7/11.2 μs	3
$MoS_2$	$max: 4.2 \times 10^4$	323		-
Si/VA-MoS <sub>2</sub>	8.75	580	10/19 μs	32
Si/VA-MoS <sub>2</sub>	0.3	808	3/40 µs	33
Si/VA-MoS <sub>2</sub>	0.908	808	56/825 ns	34
Si/VA-MoS <sub>2</sub>	7.37	532	-	35
Si/VA-MoS <sub>2</sub>	0.03	455	38.78/43.07	36
Si/VA-MoS <sub>2</sub>	0.654	980	2.1/173.8 μs	37
Si/VA-MoS <sub>2</sub>	49.31	800	80/79 ms	38
Single-layer	880	561	4/9 s	39
$MoS_2$ $FET$				
Si/Single-	7.2	365	50/50 ms	40
layer MoS2				
Si/Few-layers-	76.1	660	>50/48.9 s	41
$MoS_2$				
Si/ Thin Film-	23.1	780	21.6/65.5 μs	42
$MoS_2$				
Si/Multilayer	11.9	650	30.5/71.6 μs	43
$MoS_2$				
$Si/MoS_2 Q.D.$	2.8	514	-	44

**Table 1** outlines a comparative survey of Si-MoS<sub>2</sub> photodetector device performances. The maximal photoresponsivity reported here, 467 A/W, is found to be higher than most other devices and its characteristic response time is of  $\sim$ 12  $\mu$ s. This enhancement can be technologically beneficial for night-vision image intensifiers, working at low-light levels <sup>45</sup>. Traditionally, image intensifiers are based on intensifying tubes that convert scene photons to electrons on a photocathode; the electrons are multiplied via a multi-channel plate (MCP) and are accelerated to produce an enhanced image of the scene on a phosphorus screen. The intercalation-enhanced photodetectors may be good candidate technology for the core elements

of VIS to NIR image intensifiers, replacing bulky tubes with compact color vision. The high performance within the NIR part of the spectrum could also allow for extra imaging capabilities under low-light (photon counting) scenarios, even on moonless nights due to the atmospheric night glow phenomena. In addition, the NIR band is most suitable for imaging and analysis of high vegetation terrain (e.g. forests, agricultural fields).

#### **Conclusions**

In summary, we studied the electrical and optical properties of atomic metal-semiconductor interfaces achieved by Sn intercalation in MoS<sub>2</sub>. We found that Sn-intercalated MoS<sub>2</sub> remains semiconducting and maintains the original 2H crystal phase of the host (MoS<sub>2</sub>). The effect of intercalation on the optoelectronic properties was inferred by the measured photoresponse of Sn-intercalated MoS<sub>2</sub> photodiodes and two main features were observed: (i) non-monotonic relation of responsivity to incident power, and (ii) extension of the spectral response towards the mid-IR, far beyond the bandgap (1.2 eV) of non-intercalated MoS<sub>2</sub>. We attribute both observations to the efficient injection of hot electrons <sup>6,7</sup> and internal photoemission from midgap hybrid metal-semiconductor interface states to the conduction band of MoS<sub>2</sub>.

#### Methods

#### Sample preparation

The fabrication of CVD-grown MoS<sub>2</sub> – Si diodes is described in detail in Ref <sup>3, 46</sup>. Zerovalent Sn atoms were intercalated into the vdW gaps between the layers of VA-MoS<sub>2</sub> by a wet chemical process <sup>47</sup>. Briefly, 0.01 g of stannous chloride and 0.1g tartaric acid (Millipore-Sigma) was added to 5 mL acetone (Millipore-Sigma) in a round-bottom flask attached to a Liebig reflux condenser. The solution was brought almost to reflux at 48°C. The substrate was placed into the solution in the round-bottom flask. The solution was allowed to sit just below reflux for 4 hours, whereupon it was removed and rinsed with acetone several times. ITO and Metal contacts were finally deposited after patterning with e-beam lithography.

#### Sample characterization

#### Raman Spectroscopy

Raman spectra were obtained using a Horiba Scientific Labram HR Evolution equipped using  $\lambda = 532$  nm, solid state excitation laser, output power tuned to 0.2 mW and an optical microscope. The laser excitation propagated parallel to the crystal c-axis with linear polarization. A 50× objective lens was used to focus the laser and collect the Raman scattered light, and a 1800 groove per mm grating was chosen for spectrum acquisition.

#### FIB, HRTEM and STEM-EDS

Site-specific, cross-section FIB prepared TEM lamellae were imaged using a Probe corrected FEI Titan G2 ChemiSTEM TEM equipped with a Super-X EDX System, which comprises of four windowless silicon drift detectors of 120 mm<sup>2</sup> size, having an overall energy resolution better than 140 eV. The microscope is mounted with a Gatan 994 UltraScan 4K CCD camera, and the system has a point resolution better than 0.24 nm in the TEM mode and 80 pm in the STEM mode at 200kV accelerating voltage. The samples were imaged both in TEM and STEM

modes as well as analyzed using STEM-EDS. To avoid any stray Sn signals in the EDS spectra, appropriate care was taken and Molybdenum grids, rings and clips were used for loading the sample in the TEM holder.

The EDS data were acquired and analyzed using the Bruker QUANTAX Esprit 1.9 software. The elemental quantification was performed using the Cliff-Lorimer method with the same software.

EELS was performed using a probe-corrected Jeol JEM-ARM200F with a cold FEG source and a Gatan GIF QUANTUM spectrometer. The spectra were acquired with an energy dispersion of 0.025 eV/channel, using 2.5 mm entrance aperture.

#### Photoconductivity Measurements

The monochromatic measurements were carried out at ambient conditions under illumination of a collimated 850 nm LED<sup>3</sup>. Spectral responsivity and photocurrent were obtained by connecting the devices to an external detector socket of a Thermo Fisher Scientific NicoletiS50R. In order to obtain the Quartz-Halogen source black-body radiation curve, the source was measured using a DTGS detector. The device photocurrent spectrum was normalized to the source black-body curve to obtain the device's responsivity curve.

#### Computational Methods

Density functional theory (DFT) calculations were performed using the Vienna Ab Initio Simulation Package (VASP) 48, 49. The projector-augmented wave method 50, 51 was used to describe core and valence electrons, and electron exchange and correlation was modeled using the Perdew-Burke-Ernzerhof (PBE) generalized-gradient approximation <sup>52</sup>. The kinetic energy cutoff was set to 400 eV. Gaussian smearing of 0.05 eV was used for Brillouin zone integrations. All structural models were optimized using the conjugate-gradient method with a force tolerance of 0.01 eV/Å and an energy tolerance of 10<sup>-4</sup> eV. Both atomic positions and cell vectors were relaxed during structural optimization. To model the intercalation of Sn clusters in bulk 2H-MoS<sub>2</sub>,  $4 \times 4 \times 1$  MoS<sub>2</sub> supercells were employed; intercalation of the Sn monolayer was modeled using a single  $(1 \times 1 \times 1)$  unit cell of bulk 2H-MoS<sub>2</sub>. Van der Waals interactions were modeled using the DFT-D3 method of Grimme et al. 53 Brillouin zones of the supercells were sampled using sufficiently dense  $4 \times 4 \times 2$   $\Gamma$ -centered k-point meshes;  $16 \times 16 \times 3$  and 16 × 16 × 2 Γ-centered k-point meshes were used for the bulk MoS<sub>2</sub> primitive cell Snintercalated MoS<sub>2</sub> primitive cell, respectively. As semilocal functionals underestimate fundamental gaps, electronic structure and optical properties were calculated using the hybrid Heyd-Scuseria-Ernzerhof (HSE06)<sup>54</sup> functional. HSE calculations were performed using PBE+D3-relaxed Sn<sub>x</sub>MoS<sub>2</sub> structures (without spin-orbit coupling), as structural relaxation of these supercells with HSE is prohibitive. Electronic energies were converged to 10<sup>-6</sup> eV for calculating of optical properties. Additional details of optical calculations are provided in the supporting information.

#### **Spectral measurements and calibration**

#### Reflection measurements:

Reflection spectra were obtained using a Thermo Fisher Scientific Nicolet iS50R μFTIR. Spectral range was set to 9,000-27,000 cm<sup>-1</sup> using a Quartz-Halogen (27000-2000 cm<sup>-1</sup>) source, a Quartz beam splitter and a Silicon detector. Aperture size was set to fit the devices

aperture. A 15× objective lens was used to focus light and collect spectra from both a silver mirror as the background and the devices as the sample.

#### ASSOCIATED CONTENT

#### **Supporting Information**

The Supporting Information is available free of charge at https://pubs.acs.org/\_\_\_\_. Elemental distribution map; Electron Dispersive X-Ray Spectra; Raman Shift Characterization; Interlayer spacing and intercalation energy; Structural models; Devices production, I-V and Time Photoresponse Characterization; Spectral correlation of photoconductivity; Sample preparation and characterization (PDF).

#### Acknowledgements

AJ and AR gratefully acknowledge research funding from the U.S. National Science Foundation (NSF-BSF 1808011) and computational support from the Extreme Science and Engineering Discovery Environment (XSEDE), which is supported by National Science Foundation grant number ACI-1548562. DN would like to thank the Binational Science Foundation and U.S. National Science Foundation for jointly funding this work through grant 2017655. The authors would like to thank Yafit Pleger for assistance with FIB, for Adi Levi for technical assistance.

#### **Contributions**

CS performed CVD growth; CS fabricated the devices; KJK performed the intercalation process; CS, AT, MP performed optical/electrical measurements; DN, SS, FLD, KJK, AT, CS, AJ, AR analyzed the results; FLD, SS and IP conducted the HRTEM, STEM, EDS and EELS measurements; AT and MP conducted the spectral response measurements; AJ and AR performed the theoretical calculations and simulations; DN conceived and supervised the study; all authors read and agreed with the manuscript.

#### **Additional Information**

The authors declare no competing interest.

#### References

- 1. Jiang, R.; Li, B.; Fang, C.; Wang, J., Metal/semiconductor hybrid nanostructures for plasmon-enhanced applications. *Advanced materials* **2014**, *26* (31), 5274-5309.
- 2. Li, W.; Valentine, J. G., Harvesting the loss: surface plasmon-based hot electron photodetection. *Nanophotonics* **2017**, *6* (1), 177-191.
- 3. Stern, C.; Twitto, A.; Snitkoff, R. Z.; Fleger, Y.; Saha, S.; Boddapati, L.; Jain, A.; Wang, M.; Koski, K. J.; Deepak, F. L., Enhancing Light–Matter Interactions in MoS2 by Copper Intercalation. *Advanced Materials* **2021**, *33* (23), 2008779.
- 4. Jia, C.; Li, X.; Xin, N.; Gong, Y.; Guan, J.; Meng, L.; Meng, S.; Guo, X., Interface-engineered plasmonics in metal/semiconductor Heterostructures. *Advanced Energy Materials* **2016**, *6* (17), 1600431.
- 5. Tan, S.; Argondizzo, A.; Ren, J.; Liu, L.; Zhao, J.; Petek, H., Plasmonic coupling at a metal/semiconductor interface. *Nature Photonics* **2017**, *11* (12), 806-812.
- 6. Wu, K.; Rodríguez-Córdoba, W. E.; Yang, Y.; Lian, T., Plasmon-induced hot electron transfer from the Au tip to CdS rod in CdS-Au nanoheterostructures. *Nano letters* **2013**, *13* (11), 5255-5263.
- 7. Wu, K.; Chen, J.; McBride, J. R.; Lian, T., Efficient hot-electron transfer by a plasmon-induced interfacial charge-transfer transition. *Science* **2015**, *349* (6248), 632-635.
- 8. Tang, H.; Chen, C.-J.; Huang, Z.; Bright, J.; Meng, G.; Liu, R.-S.; Wu, N., Plasmonic hot electrons for sensing, photodetection, and solar energy applications: A perspective. *The Journal of Chemical Physics* **2020**, *152* (22), 220901.
- 9. Govorov, A. O.; Zhang, H.; Demir, H. V.; Gun'ko, Y. K., Photogeneration of hot plasmonic electrons with metal nanocrystals: Quantum description and potential applications. *Nano Today* **2014**, *9* (1), 85-101.
- 10. Briggs, N.; Bersch, B.; Wang, Y.; Jiang, J.; Koch, R. J.; Nayir, N.; Wang, K.; Kolmer, M.; Ko, W.; De La Fuente Duran, A., Atomically thin half-van der Waals metals enabled by confinement heteroepitaxy. *Nature materials* **2020**, *19* (6), 637-643.
- 11. Nisi, K.; Subramanian, S.; He, W.; Ulman, K. A.; El-Sherif, H.; Sigger, F.; Lassaunière, M.; Wetherington, M. T.; Briggs, N.; Gray, J., Light–Matter Interaction in Quantum Confined 2D Polar Metals. *Advanced Functional Materials* **2021**, *31* (4), 2005977.
- 12. Steves, M. A.; Wang, Y.; Briggs, N.; Zhao, T.; El-Sherif, H.; Bersch, B. M.; Subramanian, S.; Dong, C.; Bowen, T.; Fuente Duran, A. D. L., Unexpected Near-Infrared to Visible Nonlinear Optical Properties from 2-D Polar Metals. *Nano letters* **2020**, *20* (11), 8312-8318.
- 13. Steves, M. A.; Rajabpour, S.; Wang, K.; Dong, C.; He, W.; Quek, S. Y.; Robinson, J. A.; Knappenberger Jr, K. L., Atomic-Level Structure Determines Electron—Phonon Scattering Rates in 2-D Polar Metal Heterostructures. *ACS nano* **2021**, *15* (11), 17780-17789.
- 14. Zheng, B. Y.; Zhao, H.; Manjavacas, A.; McClain, M.; Nordlander, P.; Halas, N. J., Distinguishing between plasmon-induced and photoexcited carriers in a device geometry. *Nature communications* **2015**, *6* (1), 1-7.
- 15. Sundararaman, R.; Narang, P.; Jermyn, A. S.; Goddard III, W. A.; Atwater, H. A., Theoretical predictions for hot-carrier generation from surface plasmon decay. *Nature communications* **2014**, *5* (1), 1-8.
- 16. Li, J.; Cushing, S. K.; Meng, F.; Senty, T. R.; Bristow, A. D.; Wu, N., Plasmon-induced resonance energy transfer for solar energy conversion. *Nature Photonics* **2015**, *9* (9), 601-607.
- 17. Brown, A. M.; Sundararaman, R.; Narang, P.; Goddard III, W. A.; Atwater, H. A., Nonradiative plasmon decay and hot carrier dynamics: effects of phonons, surfaces, and geometry. *ACS nano* **2016**, *10* (1), 957-966.
- 18. Reed, B. W.; Williams, D. R.; Moser, B. P.; Koski, K. J., Chemically tuning quantized acoustic phonons in 2D layered MoO<sub>3</sub> nanoribbons. *Nano Letters* **2019**, *19* (7), 4406-4412.

- 19. Wang, M.; Lahti, G.; Williams, D.; Koski, K. J., Chemically tunable full spectrum optical properties of 2D silicon telluride nanoplates. *ACS nano* **2018**, *12* (6), 6163-6169.
- 20. Zhang, Q.; Mei, L.; Cao, X.; Tang, Y.; Zeng, Z., Intercalation and exfoliation chemistries of transition metal dichalcogenides. *Journal of Materials Chemistry A* **2020**, *8* (31), 15417-15444.
- 21. Hu, T.; Yang, D.; Hu, W.; Xia, Q.; Ma, F.; Xu, K., The structure and mechanism of large-scale indium-intercalated graphene transferred from SiC buffer layer. *Carbon* **2021**, *171*, 829-836.
- 22. Rüdorff, W., Kristallstruktur der saeureverbindungen des graphits. *Zeitschrift für Physikalische Chemie* **1940**, *45* (1), 42-68.
- 23. Mak, K. F.; Lee, C.; Hone, J.; Shan, J.; Heinz, T. F., Atomically thin MoS<sub>2</sub>: a new direct-gap semiconductor. *Physical review letters* **2010**, *105* (13), 136805.
- 24. Nerl, H. C.; Winther, K. T.; Hage, F. S.; Thygesen, K. S.; Houben, L.; Backes, C.; Coleman, J. N.; Ramasse, Q. M.; Nicolosi, V., Probing the local nature of excitons and plasmons in few-layer MoS<sub>2</sub>. *npj 2D Materials and Applications* **2017**, *1* (1), 1-9.
- 25. Rossi, T. P.; Kuisma, M.; Puska, M. J.; Nieminen, R. M.; Erhart, P., Kohn—Sham decomposition in real-time time-dependent density-functional theory: An efficient tool for analyzing plasmonic excitations. *Journal of Chemical Theory and Computation* **2017**, *13* (10), 4779-4790.
- 26. Conley, K.; Nayyar, N.; Rossi, T. P.; Kuisma, M.; Turkowski, V.; Puska, M. J.; Rahman, T. S., Plasmon excitations in chemically heterogeneous nanoarrays. *Physical Review B* **2020**, *101* (23), 235132.
- 27. Kam, K.; Parkinson, B., Detailed photocurrent spectroscopy of the semiconducting group VIB transition metal dichalcogenides. *The Journal of Physical Chemistry* **1982**, *86* (4), 463-467.
- 28. Ratchford, D. C.; Dunkelberger, A. D.; Vurgaftman, I.; Owrutsky, J. C.; Pehrsson, P. E., Quantification of efficient plasmonic hot-electron injection in gold nanoparticle—TiO2 films. *Nano letters* **2017**, *17* (10), 6047-6055.
- 29. Leenheer, A. J.; Narang, P.; Lewis, N. S.; Atwater, H. A., Solar energy conversion via hot electron internal photoemission in metallic nanostructures: efficiency estimates. *Journal of Applied Physics* **2014**, *115* (13), 134301.
- 30. Tagliabue, G.; Jermyn, A. S.; Sundararaman, R.; Welch, A. J.; DuChene, J. S.; Pala, R.; Davoyan, A. R.; Narang, P.; Atwater, H. A., Quantifying the role of surface plasmon excitation and hot carrier transport in plasmonic devices. *Nature communications* **2018**, *9* (1), 1-8.
- 31. Bernardi, M.; Mustafa, J.; Neaton, J. B.; Louie, S. G., Theory and computation of hot carriers generated by surface plasmon polaritons in noble metals. *Nature communications* **2015**, *6* (1), 1-9.
- 32. Dhyani, V.; Das, S., High-speed scalable silicon-MoS<sub>2</sub> PN heterojunction photodetectors. *Scientific reports* **2017**, *7* (1), 1-9.
- 33. Wang, L.; Jie, J.; Shao, Z.; Zhang, Q.; Zhang, X.; Wang, Y.; Sun, Z.; Lee, S. T., MoS2/Si heterojunction with vertically standing layered structure for ultrafast, high-detectivity, self-driven visible—near infrared photodetectors. *Advanced Functional Materials* **2015**, *25* (19), 2910-2919.
- 34. Qiao, S.; Cong, R.; Liu, J.; Liang, B.; Fu, G.; Yu, W.; Ren, K.; Wang, S.; Pan, C., A vertically layered MoS 2/Si heterojunction for an ultrahigh and ultrafast photoresponse photodetector. *Journal of Materials Chemistry C* **2018**, *6* (13), 3233-3239.
- 35. Majee, B. P.; Bhawna; Singh, A.; Prakash, R.; Mishra, A. K., Large area vertically oriented few-layer MoS<sub>2</sub> for efficient thermal conduction and optoelectronic applications. *The Journal of Physical Chemistry Letters* **2020**, *11* (4), 1268-1275.

- 36. Kim, H.-S.; Kumar, M. D.; Kim, J.; Lim, D., Vertical growth of MoS₂ layers by sputtering method for efficient photoelectric application. *Sensors and Actuators A: Physical* **2018**, *269*, 355-362.
- 37. Hao, L.; Gao, W.; Liu, Y.; Liu, Y.; Han, Z.; Xue, Q.; Zhu, J., Self-powered broadband, high-detectivity and ultrafast photodetectors based on Pd-MoS<sub>2</sub>/Si heterojunctions. *Physical Chemistry Chemical Physics* **2016**, *18* (2), 1131-1139.
- 38. Agrawal, A. V.; Kumar, M., Enhance near infrared performance of n-type vertically aligned MoS2 flakes photodetector with active p-type CZTS electrodes. *Materials Research Express* **2019**, *6* (11), 115011.
- 39. Lopez-Sanchez, O.; Lembke, D.; Kayci, M.; Radenovic, A.; Kis, A., Ultrasensitive photodetectors based on monolayer MoS<sub>2</sub>. *Nature nanotechnology* **2013**, *8* (7), 497-501.
- 40. Li, Y.; Xu, C.-Y.; Wang, J.-Y.; Zhen, L., Photodiode-like behavior and excellent photoresponse of vertical Si/monolayer MoS<sub>2</sub> heterostructures. *Scientific reports* **2014**, *4* (1), 1-8.
- 41. Shin, G. H.; Park, J.; Lee, K. J.; Lee, G.-B.; Jeon, H. B.; Choi, Y.-K.; Yu, K.; Choi, S.-Y., Si–MoS<sub>2</sub> vertical heterojunction for a photodetector with high responsivity and low noise equivalent power. *ACS applied materials & interfaces* **2019**, *11* (7), 7626-7634.
- 42. Lou, Z.; Zeng, L.; Wang, Y.; Wu, D.; Xu, T.; Shi, Z.; Tian, Y.; Li, X.; Tsang, Y. H., High-performance MoS<sub>2</sub>/Si heterojunction broadband photodetectors from deep ultraviolet to near infrared. *Optics letters* **2017**, *42* (17), 3335-3338.
- 43. Zhang, Y.; Yu, Y.; Mi, L.; Wang, H.; Zhu, Z.; Wu, Q.; Zhang, Y.; Jiang, Y., In Situ Fabrication of Vertical Multilayered MoS₂/Si Homotype Heterojunction for High-Speed Visible–Near-Infrared Photodetectors. *Small* **2016**, *12* (8), 1062-1071.
- 44. Mukherjee, S.; Maiti, R.; Katiyar, A. K.; Das, S.; Ray, S. K., Novel colloidal MoS<sub>2</sub> quantum dot heterojunctions on silicon platforms for multifunctional optoelectronic devices. *Scientific reports* **2016**, *6* (1), 1-11.
- 45. Bosch, L. A. In *Image intensifier tube performance is what matters*, Image Intensifiers and Applications II, SPIE: 2000; pp 65-78.
- 46. Stern, C.; Grinvald, S.; Kirshner, M.; Sinai, O.; Oksman, M.; Alon, H.; Meiron, O. E.; Bar-Sadan, M.; Houben, L.; Naveh, D., Growth mechanisms and electronic properties of vertically aligned MoS<sub>2</sub>. *Scientific reports* **2018**, *8* (1), 1-7.
- 47. Koski, K. J.; Cha, J. J.; Reed, B. W.; Wessells, C. D.; Kong, D.; Cui, Y., High-density chemical intercalation of zero-valent copper into Bi₂Se₃ nanoribbons. *Journal of the American Chemical Society* **2012**, *134* (18), 7584-7587.
- 48. Kresse, G.; Furthmüller, J., Efficient iterative schemes for ab initio total-energy calculations using a plane-wave basis set. *Physical review B* **1996**, *54* (16), 11169.
- 49. Kresse, G.; Furthmüller, J., Efficiency of ab-initio total energy calculations for metals and semiconductors using a plane-wave basis set. *Computational materials science* **1996**, *6* (1), 15-50.
- 50. Blöchl, P. E., Projector augmented-wave method. *Physical review B* **1994,** *50* (24), 17953.
- 51. Kresse, G.; Joubert, D., From ultrasoft pseudopotentials to the projector augmented-wave method. *Physical review b* **1999**, *59* (3), 1758.
- 52. Perdew, J. P.; Burke, K.; Ernzerhof, M., Generalized gradient approximation made simple. *Physical review letters* **1996,** *77* (18), 3865.
- 53. Grimme, S.; Antony, J.; Ehrlich, S.; Krieg, H., A consistent and accurate ab initio parametrization of density functional dispersion correction (DFT-D) for the 94 elements H-Pu. *The Journal of chemical physics* **2010**, *132* (15), 154104.
- 54. Krukau, A. V.; Vydrov, O. A.; Izmaylov, A. F.; Scuseria, G. E., Influence of the exchange screening parameter on the performance of screened hybrid functionals. *The Journal of chemical physics* **2006**, *125* (22), 224106.

# **Supporting Information**

# Optoelectronics of Atomic Metal-Semiconductor Interfaces in Tin-Intercalated MoS<sub>2</sub>

Avraham Twitto, <sup>1,2,†</sup> Chen Stern, <sup>1,2,†</sup> Michal Poplinger, <sup>1,2</sup> Ilana Perelshtein, <sup>2</sup> Sabyasachi Saha, <sup>4,7</sup> Akash Jain, <sup>5</sup> Kristie J. Koski, <sup>3</sup> Francis Leonard Deepak, <sup>4</sup> Ashwin Ramasubramaniam, <sup>6</sup> and Doron Naveh <sup>1,2,\*</sup>

# S1. Elemental Distribution Map

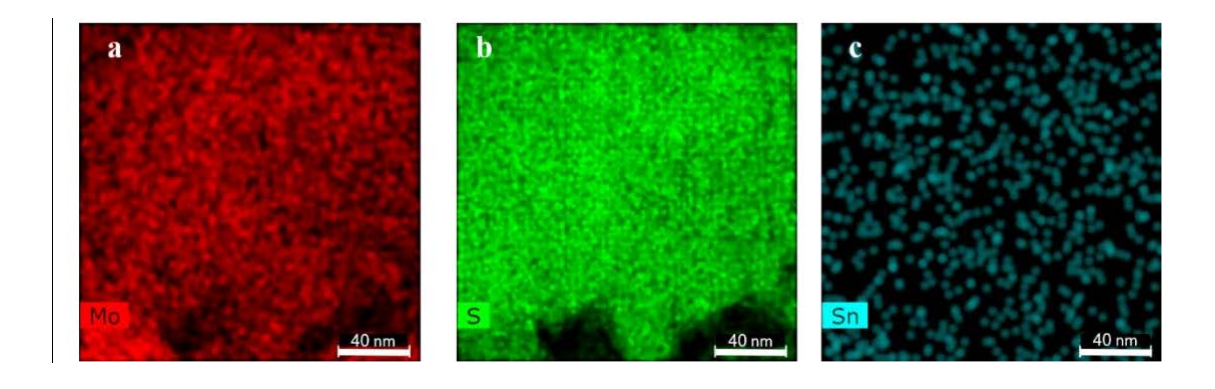


**Figure S1.** (a) Mo, (b) S and (c) Sn elemental distribution maps as collected by Energy Dispersive X-ray Spectroscopy (EDX) in TEM.

<sup>&</sup>lt;sup>1</sup> Faculty of Engineering, Bar-Ilan University, Ramat Gan, Israel

<sup>&</sup>lt;sup>2</sup> Institute for Nanotechnology and Advanced Materials, Bar-Ilan University, Ramat Gan, Israel

<sup>&</sup>lt;sup>3</sup> Department of Chemistry, University of California, Davis, USA

<sup>&</sup>lt;sup>4</sup> Nanostructured Materials Group, International Iberian Nanotechnology Laboratory, Braga, Portugal

<sup>&</sup>lt;sup>5</sup>Department of Chemical Engineering, University of Massachusetts, Amherst, MA 01003, USA

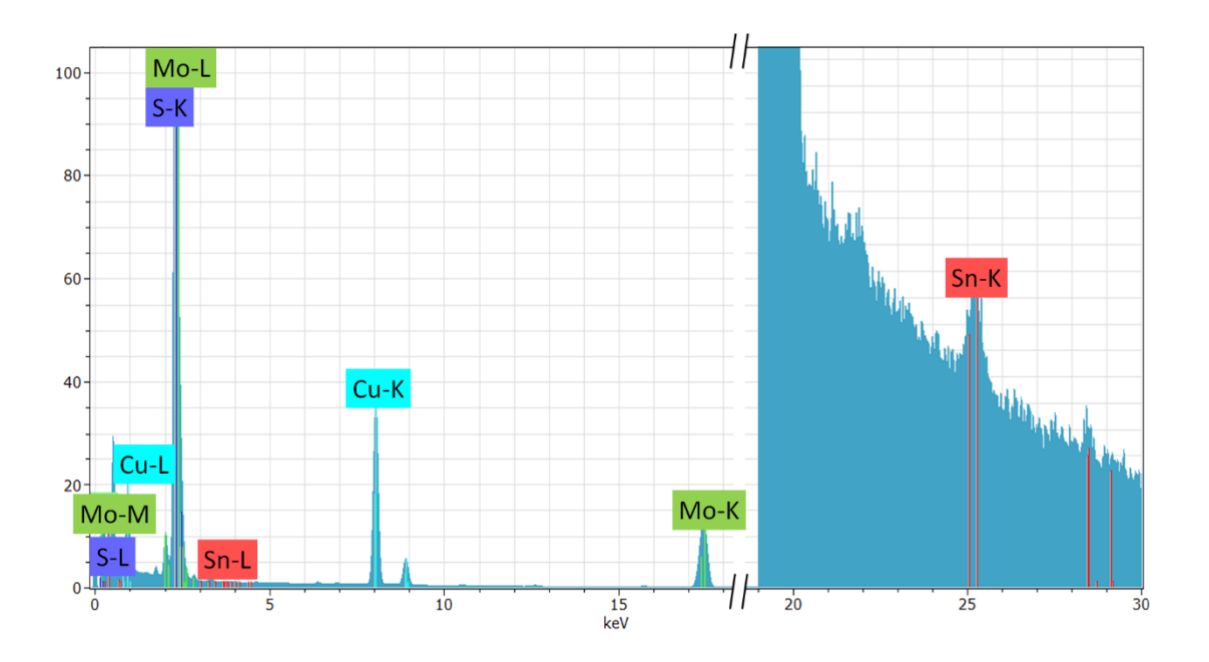
<sup>&</sup>lt;sup>6</sup> Department of Mechanical and Industrial Engineering, University of Massachusetts, Amherst, MA 01003, USA

<sup>&</sup>lt;sup>7</sup> CEMES-CNRS, 29 Rue Jeanne Marvig, 31055 Toulouse, France

<sup>\*</sup> Corresponding author: doron.naveh@biu.ac.il

<sup>&</sup>lt;sup>†</sup> The authors contributed equally to this paper.

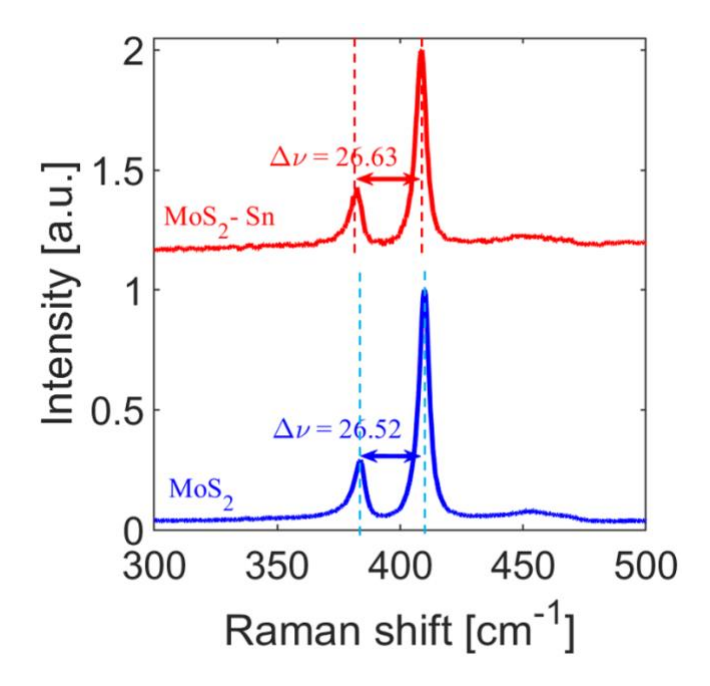
# S2. Electron Dispersive X-Ray Spectra



**Figure S2**. EDS Spectra acquired from the region within the layer of the MoS<sub>2</sub> showing Mo, S and Sn. The y-axis has been amplified 1000 times after 19keV (x-axis). It shows the presence of Sn in the MoS<sub>2</sub> layer. Cu signal is noted from the Cu grid that has been used to mount the sample.

# S3. Raman Shift Characterization

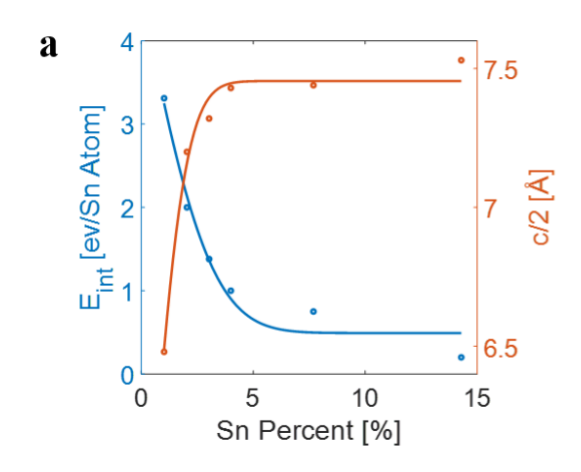
Raman spectra taken before and after intercalation show only small difference as presented in Figure S3.



**Figure S3.** Raman spectra of MoS<sub>2</sub> before (blue line) and after intercalation zero-valent Sn atoms (red line) showing characteristic spectra of 2H-MoS<sub>2</sub>.

Raman spectra were taken at a parallel geometry between the laser line and the c-axis of the crystal with linearly polarized light display the expected modes of 2H-MoS<sub>2</sub>, including an  $E^{1}_{2g}$  mode at  $\sim 383$  cm<sup>-1</sup> that corresponds to an in-plane stretch and an A1g mode at  $\sim 410$  cm<sup>-1</sup> that corresponds to an out-of-plane breathing mode  $^{1}$ . The increase in the Raman wave shift with intercalation is consistent with optical phonon stiffening and has been observed in other intercalated systems  $^{2}$ ,  $^{3}$ .

# **S4.** Interlayer spacing and intercalation energy



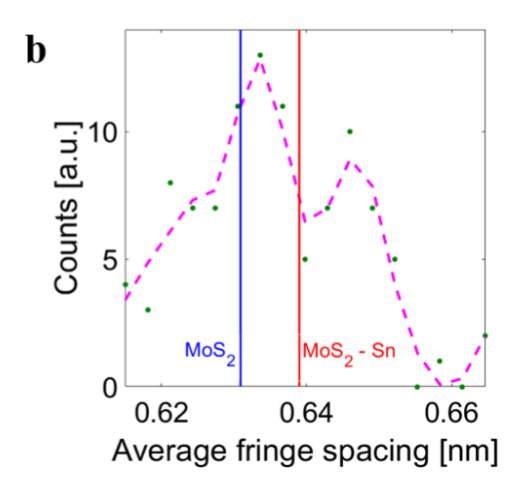


**Figure S4.** (a) Calculated energy per Sn atom ( $E_{int}$ ) required for intercalation into the vdW gap (blue symbols) and the resulting interlayer separation (c/2; orange symbols) both as functions of Sn concentration, as obtained from DFT calculations. The intercalation energy and the interlayer separation are both fitted (solid lines) to the functional form  $A \operatorname{erf}(\alpha n) + B$ , where A, B and  $\alpha$  are constants, and n is the number of atoms in an Sn cluster (see figure S4 in supporting information). Specific concentrations corresponding to the Sn<sub>ML</sub>, Sn<sub>2Cluster</sub> and Sn<sub>4Cluster</sub> models are noted in the figure. (b) Structural characterization of MoS<sub>2</sub> intercalated with zerovalent Sn atoms: Distribution and mean value of interlayer spacing between MoS<sub>2</sub> planes before (blue line) and after (red line) Sn intercalation.

The intercalation energy and the interlayer separation are both fitted to the functional form of  $A \operatorname{erf}(\alpha n) + B$ , where A, B and  $\alpha$  are constants, and n is the Sn concentration, which is proportional to the number of Sn atoms in the structure. The values for A, B and  $\alpha$  were evaluated as detailed in the following table:

	A	В	α	Goodness of fit (R-square)
E <sub>int</sub> fit	4.084	0.4913	0.2902	0.9701
c/2 fit	-2.099	7.455	0.5109	0.982

# **S5. Density functional theory modeling**

#### Structural characterization

Density functional theory (DFT) calculations were performed to gain further insights into the structural and electronic properties of the Sn-intercalated MoS<sub>2</sub> structures (Figure S5).

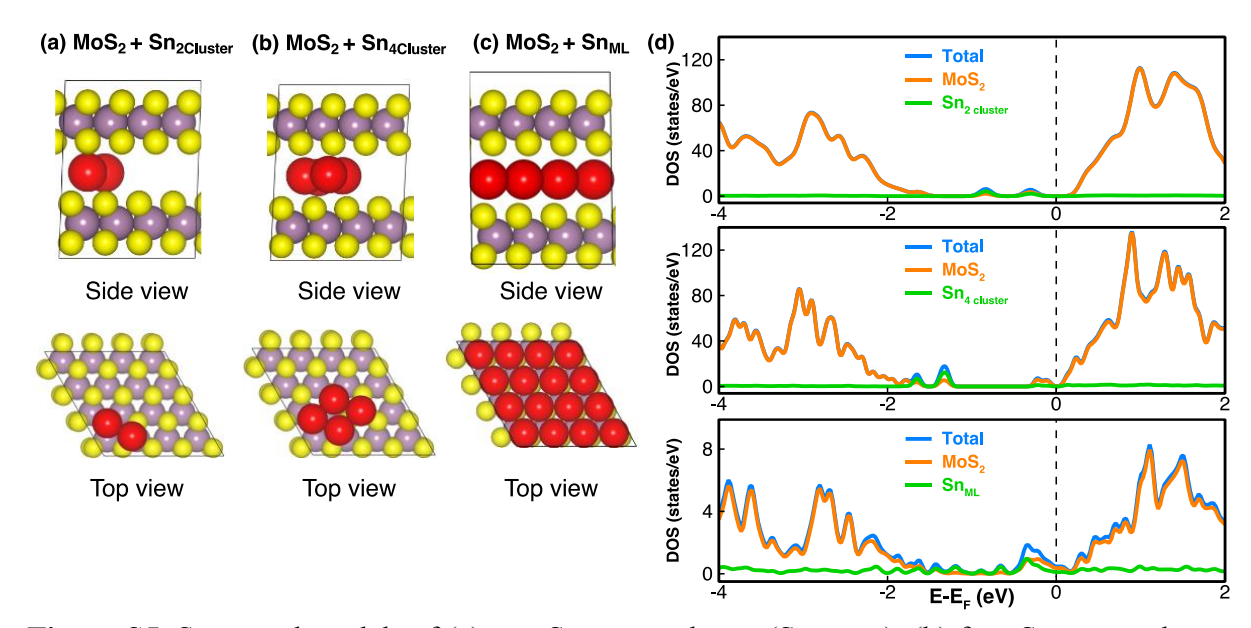


**Figure S5.** Structural models of (a) two Sn atoms cluster (Sn<sub>2Cluster</sub>), (b) four Sn atoms cluster (Sn<sub>4Cluster</sub>) and (c) a Sn monolayer (Sn<sub>ML</sub>) intercalated within a single vdW gap of bulk MoS<sub>2</sub>. One of the layers has been removed in the top views to show the intercalated Sn cluster/layer clearly. In (a) and (b), the computational supercell is indicated by solid lines; in (c) the computational unit cell consists of a single Sn atom within a vdW gap of a 1x1 cell of bulk MoS<sub>2</sub> – a 4x4 supercell of MoS<sub>2</sub>+Sn<sub>ML</sub> is displayed for clarity. (d) Density of states (DOS) of MoS<sub>2</sub>+Sn<sub>2Cluster</sub>, MoS<sub>2</sub>+Sn<sub>4Cluster</sub> and MoS<sub>2</sub>+Sn<sub>ML</sub> models calculated with the HSE functional; the total DOS (blue lines) is further decomposed into contributions from MoS<sub>2</sub> (orange lines) and Sn (green lines).

At low concentrations, individual Sn atoms bind to basal-plane sulfur atoms from both adjoining layers and are octahedrally coordinated. With increasing concentration, the Sn atoms tend to form clusters within the vdW gap (**Figure S5a, S5b**), ultimately forming continuous Sn (111) monolayers (**Figure S5b**), in agreement with the experimental observations wherein we see partial to complete layers of Sn intercalated within the MoS<sub>2</sub> vdW gap. The energetic cost of Sn intercalation (per atom),  $E_{int}$ , can be calculated as

$$E_{int} = \frac{1}{n_x} \left( E_{Sn_x MoS_2} - E_{MoS_2} - n_x E_{Sn,bulk} \right), \tag{1}$$

where x is the fraction of intercalated Sn in the Sn<sub>x</sub>MoS<sub>2</sub> structure and  $n_x$  is the total number of Sn atoms;  $E_{Sn_xMoS_2}$ ,  $E_{MoS_2}$  and  $E_{Sn,bulk}$  are the 0K DFT energies of Sn<sub>x</sub>MoS<sub>2</sub>, pristine MoS<sub>2</sub>, and a single Sn atom (bulk face-centered diamond cubic structure), respectively. As seen from **Figure S4a**, the intercalation energy is high at the outset (low Sn concentration) but decreases rapidly with increasing Sn intercalation, going from >3 eV/atom to ~0.5 eV/atom for a complete monolayer. This observation is largely similar to our prior findings for Cu intercalation in MoS<sub>2</sub> <sup>4</sup>: however, a key difference is that the intercalation energy for Cu decreases continuously whereas it rapidly saturates to a near-constant value within a few atomic percent intercalation of Sn. We ascribe this difference to the larger atomic size of Sn, as compared to Cu; such that once a small fraction of Sn atoms is "wedged" into the MoS<sub>2</sub> vdW gap, the intercalation of additional Sn becomes relatively facile. This intuition is also borne out by the expansion of the interlayer spacing (**Figure S4**) which rapidly increases from 6.17 Å in pristine MoS<sub>2</sub> and saturates to 7.4–7.5 Å within a few atomic percent of Sn being intercalated; in contrast, the interlayer spacing was found to increase continuously for Cu intercalation <sup>4</sup>.

The electronic density of states of the  $Sn_xMoS_2$  models are displayed in **Figure S5d** from which we notice two key features: (a) a shift in the Fermi level towards the conduction band edge of  $MoS_2$  (n doping  $\sim 10^{22}$  e<sup>-</sup>/cm<sup>3</sup> for the Sn monolayer), and (b) the emergence of gap states within the  $MoS_2$  band gap that have contributions from both the  $MoS_2$  layers and the intercalated Sn clusters/layer. At lower concentrations of intercalated Sn (Sn<sub>2</sub> cluster), the gaps states appear mid-gap; with increasing Sn intercalation (Sn<sub>4</sub> cluster) these gap states begin to merge gradually with the band edges. Once the intercalated Sn forms a complete monolayer, we observe a significant density of states within the original  $MoS_2$  band gap—some of these additional states appear as sharp resonances while others appear as a broader continuum; it is noteworthy that the overall hybrid structure is still semiconducting with a small gap  $\sim 0.1$  eV visible at the conduction band edge (**Figure S5d**).

#### **Optical properties**

The frequency-dependent dielectric functions of various  $Sn_xMoS_2$  models were calculated within the independent-particle approximation. To converge the low-energy features we used denser k-point meshes of  $30 \times 30 \times 2$  for  $MoS_2+Sn_{ML}$  and  $50 \times 50 \times 1$  for  $Sn_{ML}$ . The Fock operator was reduced by a factor of two in plane to accelerate the calculations without loss of accuracy. **Figure S6** displays the real  $(\varepsilon_1)$  and imaginary  $(\varepsilon_2)$  components of the dielectric

function as well as the EELS spectra for MoS<sub>2</sub>+Sn<sub>ML</sub>, bulk MoS<sub>2</sub>, and Sn<sub>ML</sub>. The structural model for Sn<sub>ML</sub> was created by freezing the Sn atoms at their equilibrium positions in the MoS<sub>2</sub>+Sn<sub>ML</sub> model and eliminating the MoS<sub>2</sub>. This fictitious configuration, while not the ground state of a Sn monolayer, allows us to probe more directly the contribution of the Sn atoms to the overall optical response of the hybrid structure. Plasmonic features in the EELS spectrum are identified by associating them with zero crossings with positive slope of  $\varepsilon_1$ . <sup>5-8</sup> As seen from **Figure S6**, there are weak plasmonic features that appear as shoulders in the EELS spectrum of MoS<sub>2</sub>+Sn<sub>ML</sub>: the more prominent of these features is near 1.1 eV while a less prominent one occurs close to 1.6 eV. It should be noted that there are no such plasmonic features in the EELS spectra of bulk MoS<sub>2</sub> within the same energy window (0.5–2.6 eV), thus clearly indicating that the plasmons of MoS<sub>2</sub>+Sn<sub>ML</sub> are an emergent property of the hybrid material.

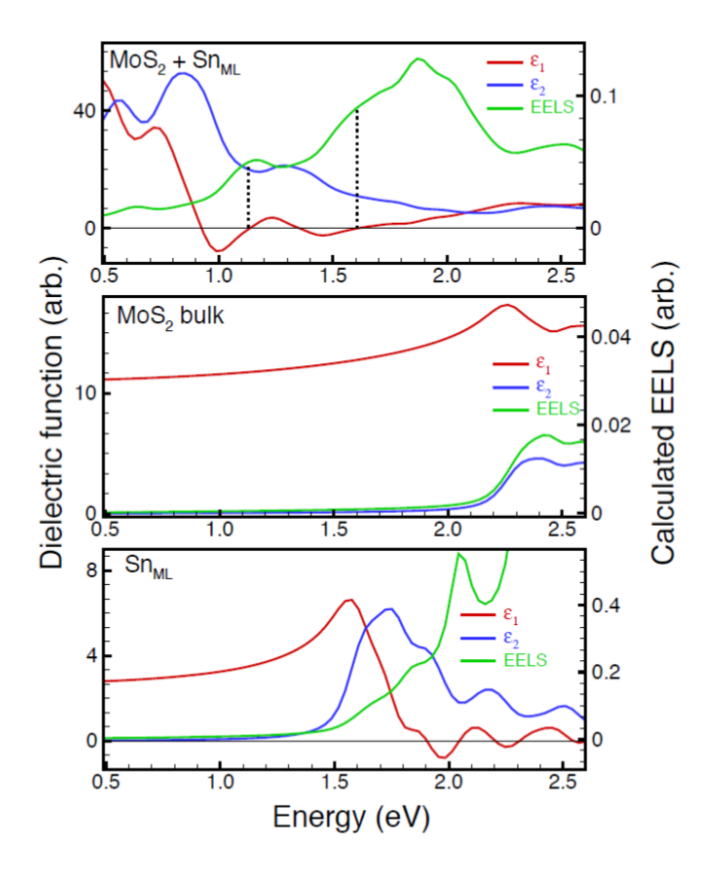


**Figure S6.** Calculated dielectric functions and EELS for MoS<sub>2</sub>+Sn<sub>ML</sub> (top), bulk MoS<sub>2</sub> (middle) and constrained Sn<sub>ML</sub> (bottom). Vertical dashed lines correlate zero crossings with positive slope of  $\varepsilon_1$  with plasmonic features in the EELS spectrum. Only the low energy part of the spectrum is plotted here to display and compare the plasmonic features of interest.

## S7. Devices production, I-V and Time Photoresponse Characterization

In order to examine the optoelectronic activity of Sn intercalated MoS<sub>2</sub> diodes (see graphical illustration in **Figure 2a** and device cross section in **Figure 2b**), the I-V transfer curves were measured in dark and illuminated with a 850 nm wavelength light source at varying power, as shown in Figure S6a and S6b. In addition, the response time was measured is displayed in **Figure S7c**, as recorded from devices of bare and intercalated MoS<sub>2</sub> operated with a 20 kHz modulated light source and at voltage bias of -2V.

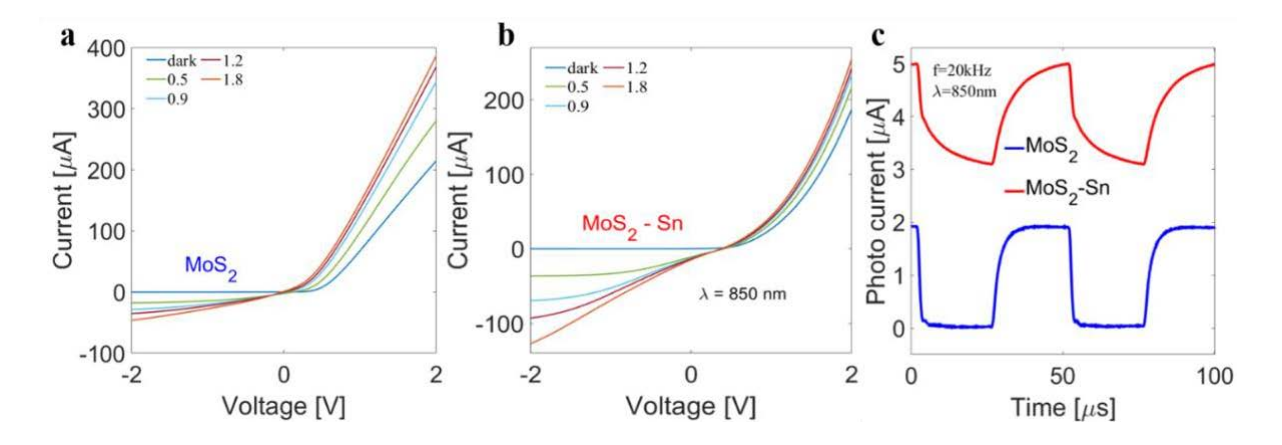


**Figure S7.** (a) I-V photoresponse curve in linear scale of the bare MoS<sub>2</sub> at different power illuminations ( $\mu$ W). in 850 nm. (b) I-V photoresponse curve in linear scale of the Sn-MoS<sub>2</sub> at different power illuminations ( $\mu$ W) at wavelength of 850 nm. (c) Time dependent photoresponse of MoS<sub>2</sub> (blue), and Sn intercalated MoS<sub>2</sub> devices (red) illuminated at  $\lambda$  = 850 nm,  $P_{in}$  = 1.5  $\mu$ , under reverse bias of -2V.

# **S8.** Spectral Correlation of Photoconductivity

Comparison between the devices measured Responsivity, Calculated Absorption and EELS is presented in **Figure S8**. The same data appears in the manuscript in **Figure 2a**, **Figure 2e** and **Figure 3b**.

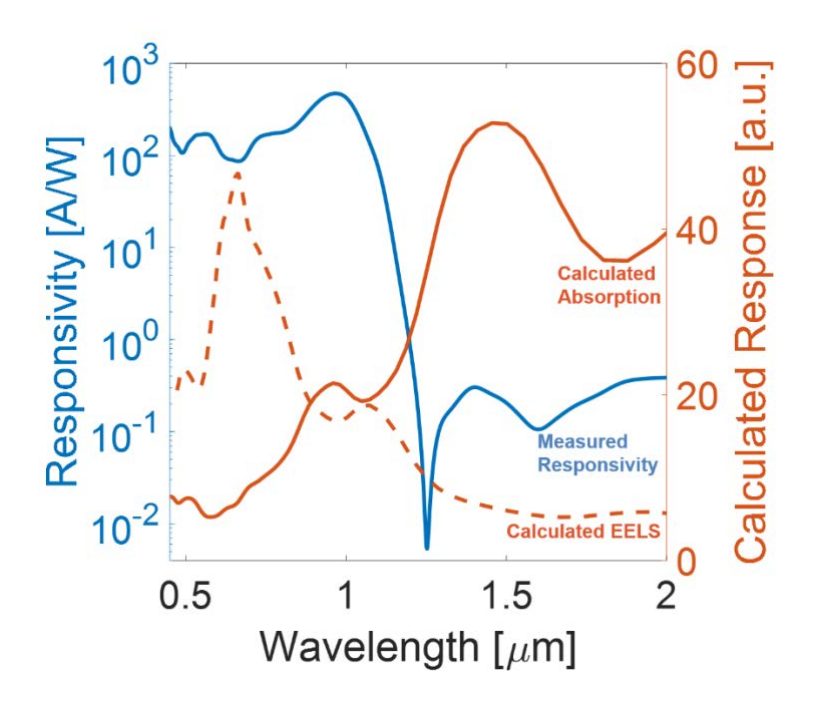


**Figure S8.** Responsivity (blue left y axis), Calculated Absorption (orange solid line, right y axis), Calculated EELS (orange dashed line, right y axis).

## **References**

- 1. Li, H.; Zhang, Q.; Yap, C. C. R.; Tay, B. K.; Edwin, T. H. T.; Olivier, A.; Baillargeat, D., From bulk to monolayer MoS<sub>2</sub>: evolution of Raman scattering. *Advanced Functional Materials* **2012**, *22* (7), 1385-1390.
- 2. Reed, B. W.; Williams, D. R.; Moser, B. P.; Koski, K. J., Chemically tuning quantized acoustic phonons in 2D layered MoO<sub>3</sub> nanoribbons. *Nano Letters* **2019**, *19* (7), 4406-4412.
- 3. Wang, M.; Lahti, G.; Williams, D.; Koski, K. J., Chemically tunable full spectrum optical properties of 2D silicon telluride nanoplates. *ACS Nano* **2018**, *12* (6), 6163-6169.
- 4. Stern, C.; Twitto, A.; Snitkoff, R. Z.; Fleger, Y.; Saha, S.; Boddapati, L.; Jain, A.; Wang, M.; Koski, K. J.; Deepak, F. L., Enhancing Light–Matter Interactions in MoS<sub>2</sub> by Copper Intercalation. *Advanced Materials* **2021**, *33* (23), 2008779.
- 5. Pines, D.; Collective Energy Losses in Solids. Reviews of Modern Physics 1956, 28 (3), 184-198.
- 6. Keast, V. J.; Ab Initio Calculations of Plasmons and Interband Transitions in the Low-Loss ELectron Energy-Loss Spectrum. *Journal of Electron Spectroscopy and Related Phenomena* **2005**, 143, 97-104.
- 7. Andersen, K.; Jacobsen, K. W.; Thygesen, K. S., Spatially resolved quantum plasmon modes in metallic nano-films from first-principles. *Physical Review B* **2012**, 86, 245129.
- 8. Lajaunie, L.; Boucher, F.; Dessapt, R.; Moreau, P., Strong anisotropic influence of local-field effects on the dielectric response of α-MoO<sub>3</sub>. *Physical Review B* **2013**, 88, 115141.